Active acoustic metamaterials with on-demand bulk modulus and full mass density tensor

To cite this article: Dylan A Kovacevich and Bogdan-Ioan Popa 2024 *Smart Mater. Struct.* **33** 105012

OPEN ACCESS
IOP Publishing
Smart Materials and Structures
Smart Mater. Struct. **33** (2024) 105012 (9pp)
https://doi.org/10.1088/1361-665X/ad7550

Active acoustic metamaterials with on-demand bulk modulus and full mass density tensor

Dylan A Kovacevich and Bogdan-Ioan Popa*

Department of Mechanical Engineering, University of Michigan, Ann Arbor, MI 48109, United States of America

E-mail: bipopa@umich.edu

Received 7 July 2024, revised 23 August 2024
Accepted for publication 29 August 2024
Published 6 September 2024

Abstract

Active metamaterials address fundamental limitations of passive media and have widely been recognized as necessary in numerous compelling applications such as cloaking and extreme noise absorption. However, most practical devices of interest have yet to be realized due to the lack of a suitable strategy for implementing bulk active metamaterials—those that involve interacting cells and functionality beyond one dimension. Here, we present such an active acoustic metamaterial design with bulk modulus and anisotropic mass density that can be independently programmed over wide value ranges. We demonstrate this ability experimentally in several examples, targeting acoustic properties that are hard to access otherwise, such as a bulk modulus significantly smaller than air, strong mass density anisotropy, and complex bulk modulus and mass density for high reflectionless sound absorption. This work enables the transition of active acoustic metamaterials from isolated proof-of-concept demonstrations to versatile bulk materials.

Supplementary material for this article is available online

Keywords: acoustics, metamaterials, active metamaterials, transformation acoustics, anisotropy

1. Introduction

In acoustics, the bulk modulus κ and the mass density tensor $\boldsymbol{\rho}$ are the primary properties that dictate the propagation of sound waves. Manipulations of the acoustic wave equation and its solutions, such as by transformation acoustics [1, 2], reveal the extent to which we can control the propagation of sound by varying these properties in space. They have inspired the design of devices such as waveguides/beam steerers [3–5], lenses [6–8], and cloaks [9–12] with great potential applications in areas like noise management and remote sensing/imaging. However, the acoustic property specifications of many of these devices are highly demanding, including κ and $\boldsymbol{\rho}$ much smaller and larger than the incident wave-bearing medium, strong anisotropy, and steep spatial gradients. Conventional materials do not readily possess such acoustic properties, necessitating the development of a new class of materials, namely metamaterials. The foundation of the metamaterials design strategy is that media composed of highly subwavelength unit cells behave identically to continuous materials, but can be engineered to have extraordinary effective properties. These properties can be evaluated from scattering behaviour, such that if a metamaterial and continuous material produce the same scattered field for any external excitation, they are characterized by the same effective properties. In isolation, metamaterial unit cells have been designed with the properties

* Author to whom any correspondence should be addressed.

needed for transformation acoustics, but attempts to satisfy full property maps requiring many cells and realize practical devices have fallen short.

Much of past effort focused on the design of metamaterials composed of resonant composite structures because their properties can be far beyond those of their constituent materials [13–16]. However, this approach suffers from several fundamental drawbacks, including narrow bandwidth and high loss, as well as challenges of fabrication, such as the unwanted coupling of properties and the difficulty of integrating different unit cell architectures. Non-resonant metamaterials face the same issues, but trade a significantly diminished range of achievable properties for a broader bandwidth [15, 16]. For example, without resonance, solid-air composite metamaterials cannot achieve an effective mass density less than that of air. Transformation acoustics devices such as cloaks have been fabricated with non-resonant metamaterials using relaxed property specifications [17–20], but these adjustments, coupled with loss from narrow channels, resulted in significantly degraded performance (e.g. substantial scattering from cloaks).

An alternative approach, active metamaterials, has shown the potential to overcome the obstacles faced by passive composite metamaterials. Active unit cells consist of electronically paired sensors and drivers that produce a programmed response to the local field. Each cell operates independently, so the metamaterials can be scaled to an arbitrary number of active elements, unlike in conventional active systems that require centralized control. With a suitable programming strategy, active metamaterials can be designed to generate scattered fields identical to those of continuous physical media with desired effective properties. Previous works on active acoustic metamaterials utilized pressure and particle velocity sensors paired with monopole and dipole drivers. This setup was used to experimentally achieve metamaterials of programmable bulk modulus [21, 22] and mass density in one direction [21–23], as well as a variety of other characteristics such as Willis coupling [24–27], non-reciprocity [25–30], anomalous reflection [31], amplification [27, 32], wavelength down-conversion [33], and spatiotemporal modulation [32, 34]. Similar works can also be seen in the elastic domain [35–38].

Crucially, these demonstrations were primarily limited to one-dimensional operation with only a single cell, a row of a few cells, or other arrangement of non-interacting cells. Moreover, the effective properties were typically characterized experimentally after the design, through a two-port scattering matrix method for example, rather than being predictably programmed. Devices of many cells with wave propagation through the bulk have not been realized due to the lack of a model for the complex interactions between cells and the programming strategy necessary to obtain specified effective properties. We addressed these theoretical challenges in our previous work on a polarized source model [39], which relates the scattering of subwavelength fluid cylinders to that of active acoustic metamaterial unit cells with programmable bulk modulus and mass density tensor. With a design based on this model, we experimentally implemented six rectangularly arranged cells with programmable κ and two-dimensional (2D) operation [40]. However, this metamaterial required only a single sensor and driver in each cell, making it far easier to realize than one with a full set of programmable material properties, as has yet to be achieved.

In this work, we experimentally demonstrate an active acoustic metamaterial with individually programmable κ and $\boldsymbol{\rho}$ tensor elements with 2D operation. We show in several examples that this metamaterial is an excellent building block for transformation acoustics and noise absorption devices. These examples include the realization of effective κ and $\boldsymbol{\rho}$ components both smaller and larger than the background medium (air), and anisotropic $\boldsymbol{\rho}$ with principal axes rotated by a prescribed angle purely through programming. We also demonstrate a highly absorbing medium having a speed of sound c with a large loss component and background-matched characteristic impedance z such that incident waves are absorbed without reflection. The cells composing the metamaterial can be arranged in arbitrary geometries and programmed independently to directly match prescribed effective property maps. Here, we choose to demonstrate nine cells programmed with identical properties and arranged in a square, presenting the challenge of having the cells strongly interacting with each other. We describe the cell architecture and programming strategy for desired effective properties, which we validate by comparing the 2D total and scattered fields of the experimental active metamaterial to those of ideal simulated media. These fields are shown at a single frequency, but the metamaterial does not rely on resonance and could in theory be designed to have large bandwidths by tailoring the programmed frequency responses and reducing system lag. In total, this active metamaterial design promises previously unobtainable acoustic properties on-demand, enabling the realization of extreme wave control devices that are too difficult to fabricate using passive structures, as well as those that require reconfigurability for dynamic applications.

2. Design and experimental methods

2.1. Metamaterial design

We aim to experimentally realize a bulk medium with 2D geometry and fully programmable acoustic properties κ and $\boldsymbol{\rho}$ by embedding an active acoustic metamaterial in the lower plate of a 2D waveguide, as modeled in figure 1(a). Our design strategy is for each unit cell of the metamaterial to have the sensors, drivers, and programming that is necessary to replicate the acoustic behavior of a highly subwavelength fluid cylinder, producing the same scattering as one for any incident wave, as in figure 1(b). The active metamaterial of many such cells will then act as an array of fluid cylinders in a background medium, with interactions between cells identical to the scattering between cylinders. Because the cells are subwavelength, the metamaterial can be homogenized as a continuous medium and described by acoustic properties that are programmable through the properties of the constituent cylinders.

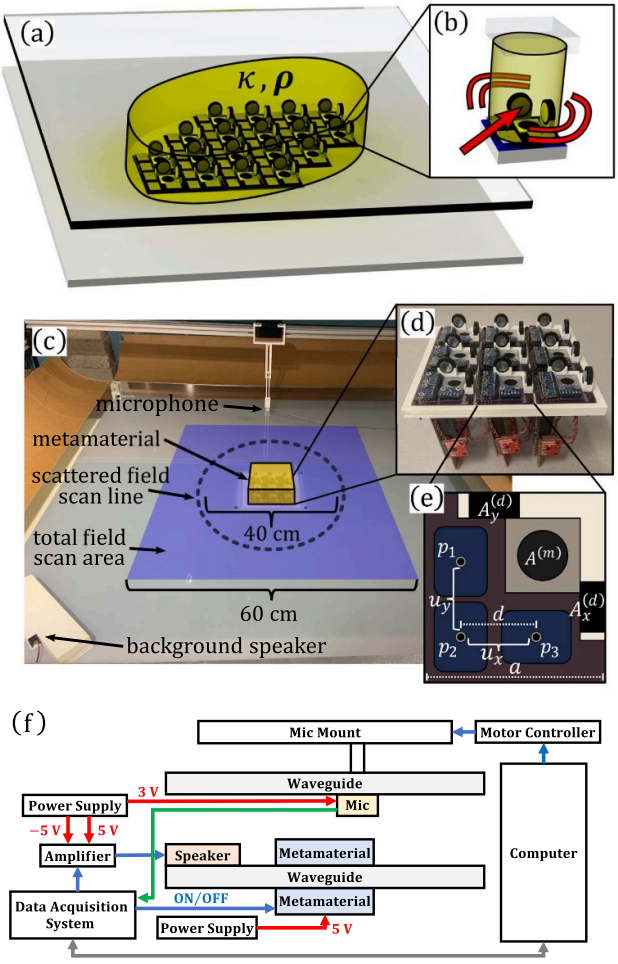

Figure 1. (a) An active acoustic metamaterial in a 2D waveguide used to realize an effective medium with arbitrary geometry and programmable acoustic properties. (b) A single active unit cell scatters sound as if it were a subwavelength fluid cylinder. (c) Experimental setup with a background speaker that ensonifies the metamaterial and a microphone on a motorized mount that scans the waveguide interior to measure the background and total pressure. (d) Metamaterial consisting of a 3×3 arrangement of cells, each with a controller hidden underneath the waveguide lower plate when mounted. (e) Diagram of a unit cell from a top-down view. (f) Experimental setup block diagram with electrical connections between devices.

The experimental 2D waveguide setup shown in figure 1(c) with peripheral devices diagrammed in figure 1(f) was used to evaluate the acoustic behavior of a square active metamaterial sample of nine cells shown in figure 1(d). Each cell consists of two printed circuit boards (PCBs), one with its surface flush to the frame and another that hangs perpendicularly underneath. The upper PCB, diagrammed from a top-down view in figure 1(e), supports the sensor (Adafruit, SPH0645LM4H) and driver (PUI Audio, AS01508MR-6-LW100-R) elements, while the lower PCB supports a microcontroller (PJRC, Teensy 4.0) and amplifiers (SparkFun, MAX98357A). For testing, the metamaterial was mounted in the lower plate of the 2D waveguide, such that only the upper PCB components interfaced with, but negligibly scattered (see supplementary note 1), incident waves.

Each unit cell (refer to figure 1(e)) has three speakers as the driving elements and three microphones as the sensing elements. The speakers are oriented along perpendicular axes, with the two directed in the plane of the 2D waveguide acting as dipole sources with amplitudes $A_x^{(d)}$ and $A_y^{(d)}$, while the third acts as a monopole source with amplitude $A^{(m)}$ (the upper PCB and lower waveguide plate act as a baffle). The microphones are arranged at the vertices of a right triangle with legs along the x- and y-directions. The pressures they sense, labeled as p_1, p_2, and p_3 in figure 1(e), can be used to determine the local pressure p_{loc} and particle velocity components $u_{\text{loc},x}$ and $u_{\text{loc},y}$ in the time domain as,

$$\begin{aligned} p_{\text{loc}} &= \frac{1}{3}\left(p_1 + p_2 + p_3\right), \\ u_{\text{loc},x} &= -\frac{1}{\rho_0 d}\int \left[p_2 - p_3\right] \mathrm{d}t, \\ u_{\text{loc},y} &= -\frac{1}{\rho_0 d}\int \left[p_2 - p_1\right] \mathrm{d}t. \end{aligned} \tag{1}$$

The local pressure is the average pressure of the three microphones. The particle velocities are calculated as the integral with respect to time of the pressure difference between microphone pairs, with a coefficient including the mass density of the background medium ρ_0 and the microphone spacing $d = 1.5$ cm.

To enact our desired acoustic behavior, we programmed the unit cells using an open loop control strategy that relates the speaker amplitudes to the sensed quantities by five transfer functions g,

$$A^{(m)} = g^{(m)} p_{\text{loc}}, \quad \begin{bmatrix} A_x^{(d)} \\ A_y^{(d)} \end{bmatrix} = \begin{bmatrix} g_x^{(d)} & g_{xy}^{(d)} \\ g_{yx}^{(d)} & g_y^{(d)} \end{bmatrix} \begin{bmatrix} u_{\text{loc},x} \\ u_{\text{loc},y} \end{bmatrix}. \tag{2}$$

The parenthesized superscript of a transfer function g denotes its association with a monopole (m) or dipole (d) driver (same as in the amplitudes). The subscripts indicate the directional components, with the driven component followed by the sensed component when the directions are different. The transfer functions, for which we are only interested in the steady-state behavior, each include the built-in frequency responses of the electronic and acoustic elements, as well as a band-pass filter and gain that were digitally implemented through the microcontroller. To achieve a specific set of desired acoustic properties, solely the gains, which include magnitude and delay components, were adjusted. Their values were chosen to obtain the overall transfer functions g that, at the target operating frequency, match the ideal magnitude and phase specified by a polarized source model of subwavelength fluid cylinders [39]. As the fluid cylinders are not resonant, the properties of one cell, and therefore its necessary programming, does not depend on the properties of its neighbors. The ideal transfer functions with which to program a unit cell for desired κ and $\boldsymbol{\rho}$ will be written explicitly in section 3. Further details about the metamaterial electronic components and digital processing can be found in supplementary notes 3 & 4 respectively.

2.2. Experimental acoustic field measurement

Experiments to characterize the active acoustic metamaterial properties through its scattering behavior were performed in the 2D waveguide with side length of 100 cm and plate spacing of 6 cm shown in figure 1(c). For each experiment, the gains g of all nine cells were programmed identically so that the metamaterial would act as a homogeneous medium with desired properties κ and $\boldsymbol{\rho}$. While the cells could be programmed differently to achieve spatially varying properties, we limit our demonstrations to homogeneous media for clarity given the small metamaterial size. A speaker at the edge of the waveguide was commanded with a pulse of trapezoidal bounding amplitude and center frequency of 1200 Hz (wavelength in air of 29.6 cm) to produce a background wave in the fundamental mode that ensonified the metamaterial. The speaker was oriented at angles of $0, 45$, and 90° to demonstrate that the metamaterial behaves as the desired effective medium for both normal and oblique incidence. A microphone magnetically suspended underneath the top waveguide plate on a motorized mount was used to measure the background field with the metamaterial off, followed by a measurement of the total field with the metamaterial on. The difference of measurements is the scattered pressure that was generated by the metamaterial. Measurements were made in a square grid centered on the metamaterial with 2 cm spacing and 60 cm side length, spanning the purple region in figure 1(c). The Fast Fourier Transform of each experimentally measured time-domain signal was taken in the constant amplitude window of the incident wave, yielding the spatially-varying magnitude and phase of the total and scattered fields at 1200 Hz. An advantage of the metamaterial not physically occluding the waveguide is that the acoustic field can actually be measured within the effective material domain in addition to the typical external measurements, providing further insight into the metamaterial behavior.

2.3. Comparison to ideal behavior

All experimentally obtained total and scattered fields are compared to ideal fields calculated from modeling the metamaterial unit cells as polarized sources [39] responding to the experimental background pressure data. The ideal scattered fields are purely simulated, while the ideal total fields are the superposition of the ideal scattered fields and the experimental background fields. The polarized source model has been shown to produce the same results as finite element method simulations of continuous media, with general examples in [39] and validation for some of the specific cases here in supplementary note 2. Therefore, if the experimental and simulated fields match, we can say that the metamaterial behaved as if it was a continuous medium with the target effective acoustic properties in the path of the incident wave. In section 3, the total field magnitudes are presented as surface plots, normalized by the background pressure at the center of the metamaterial. The associated total field phases can be found in supplementary note 5. The scattered fields were interpolated along the 40 cm diameter circular slice shown in figure 1(c) and are presented as polar plots, with one for magnitude (same normalization as the surface plots) and one for phase.

3. Results

3.1. Tunable bulk modulus

The metamaterial bulk modulus κ can be programmed through the pairing of each unit cell's monopole speaker amplitude $A^{(m)}$ with its locally sensed pressure p_{loc}. From the polarized source model [39, 40], the ideal transfer function relating the sensed and driven quantities is,

$$g^{(m)} = (k_0 a/2)^2 \left(1 - \frac{1}{\kappa_{\text{eff}}}\right), \tag{3}$$

where κ_{eff} is the metamaterial effective bulk modulus defined relative to the bulk modulus of the background medium air κ_0 such that $\kappa = \kappa_{\text{eff}}\kappa_0$. The wavenumber in air is k_0 and the side length of an active unit cell is $a = 4.6$ cm (six cells per wavelength at 1200 Hz).

To showcase the ability to program the metamaterial κ for specific values both less than and greater than the background medium, as needed for transformation acoustics, we experimentally demonstrated the metamaterial with each κ_{eff} in the set $\{0.6, 0.8, 1.3, 2\}$. All nine cells of the metamaterial were individually programmed with the same $g^{(m)}$ to achieve the desired κ_{eff}. According to equation (3), the $g^{(m)}$ for $\kappa_{\text{eff}} < 1$ has 180° phase and magnitude that increases as κ_{eff} approaches zero. The $g^{(m)}$ for $\kappa_{\text{eff}} > 1$ has 0° phase and magnitude that increases as κ_{eff} approaches infinity. The sub-unity values of κ_{eff} are very challenging to achieve with conventional methods. For example, broadband passive metamaterial realizations require a material constituent with bulk modulus less than that of air, but the typical inclusions are solids, which do not possess this property.

For each programmed property, the metamaterial was ensonified by an approximate plane wave at 45° in the 2D waveguide (setup of figure 1(c)). The resultant total pressure magnitudes are shown in figure 2(a), with experimental data for each κ_{eff} in the left column compared to the ideal simulated data in the right column. The features of the fields are a strong match throughout the measured region. Remarkably, this match is maintained inside the metamaterial domain. As an alternative visualization where error may be more easily quantified, the scattered pressure fields along a circular slice are shown in figure 2(b). The experimental results are plotted as solid lines with color indicating the κ_{eff} and simulated results as dotted lines of a slightly darker shade. In angular sections where the scattered field is of near-zero magnitude (see $\kappa_{\text{eff}} \in \{0.6, 0.8\}$), the phase was not plotted as it cannot accurately be determined for the experimental results (e.g. at vanishingly small amplitudes, all phase values produce the same results). The scattered magnitudes are larger for the κ_{eff} further from the background and the phases are grouped by $\kappa_{\text{eff}} < 1$ and $\kappa_{\text{eff}} > 1$ as expected from equation (3). Due to

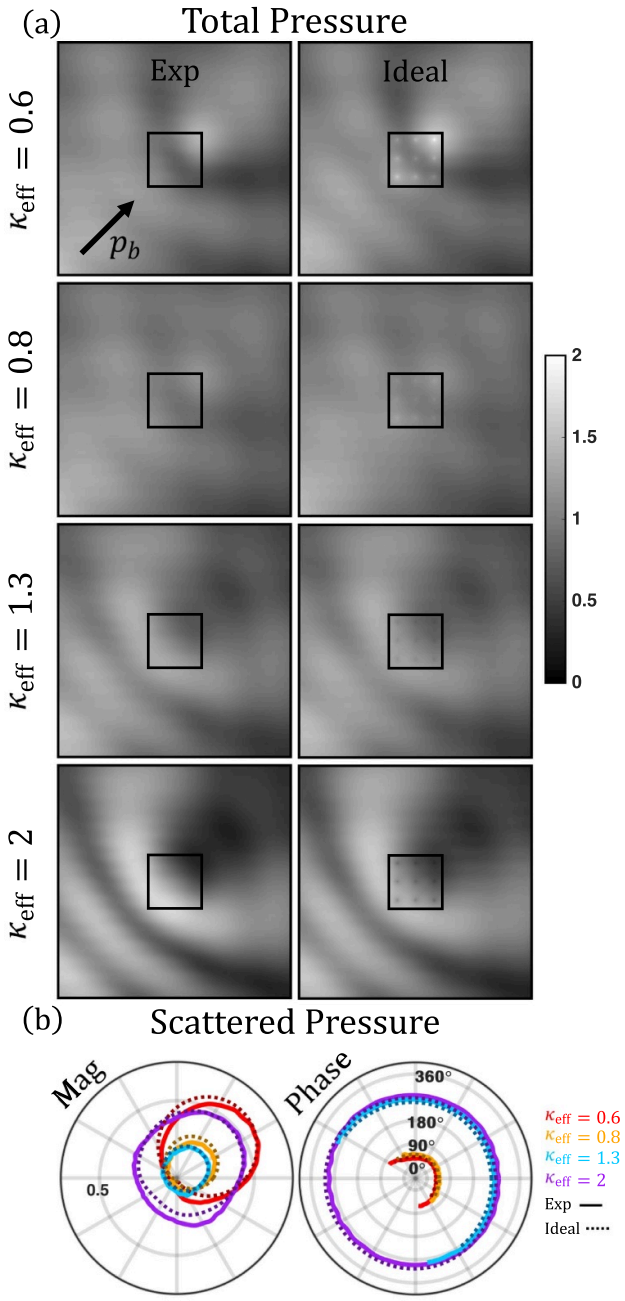

Figure 2. Comparison of experimental and simulated ideal pressure fields due to a 45° background wave incident on the metamaterial programmed with each κ_{eff} in the set $\{0.6, 0.8, 1.3, 2\}$. (a) Total pressure magnitudes in a 60 cm square area with the metamaterial indicated by a black outline. (b) Scattered pressure magnitudes and phases along a 40 cm diameter circle centered on the metamaterial.

the full metamaterial size being only half a wavelength, the scattered field magnitudes mostly maintain the single lobe characteristic of a monopole source. The experimental and ideal results are in great agreement for both the magnitude and phase components, demonstrating that the active response of the metamaterial is equivalent to the scattering of a continuous medium with the desired effective properties.

3.2. Diagonal anisotropic mass density tensor

The metamaterial can be programmed with a diagonal mass density tensor $\widetilde{\boldsymbol{\rho}}$ with Cartesian principal axes through transfer functions $g_x^{(d)}$ and $g_x^{(y)}$ that independently dictate $\rho_{\text{eff},x}$ and $\rho_{\text{eff},y}$. These transfer functions relate the dipole speaker amplitudes $A_x^{(d)}$ and $A_y^{(d)}$ to the particle velocities sensed in their corresponding directions $u_{\text{loc},x}$ and $u_{\text{loc},y}$, as in equation (2). The ideal programming from the polarized source model is [39],

$$g_{x(y)}^{(d)} = z_0 (k_0 a/2)^2 \left[\frac{1 - h\left(\rho_{\text{eff},x(y)}\right)}{1 + h\left(\rho_{\text{eff},x(y)}\right)} \right] \tag{4}$$

where z_0 is the characteristic impedance of the background medium and h is a function for the mass density of a sub-wavelength fluid cylinder given the effective mass density of a homogenized square-packed array of such cylinders. Here, h was obtained from finite element simulations using scattering matrix characterization [39].

For an experimental demonstration, the metamaterial was programmed with $\widetilde{\boldsymbol{\rho}}$ components of $\rho_{\text{eff},x} = 0.5$ and $\rho_{\text{eff},y} = 1.5$. The background speaker was positioned to ensonify the metamaterial at 45°, followed by the x- and y-directions. This set of incident waves enables us to see both the asymmetric scattering due to anisotropy and the symmetric scattering corresponding to the isolated density components. The total pressure magnitudes are shown in figure 3(a), with experimental data for each direction of incidence in the left column compared to the ideal simulated data in the right column. The scattered pressure fields are shown in figure 3(b), with $\theta = 0°$ indicating incidence in the x-direction and $\theta = 90°$ indicating incidence in the y-direction. Both the total and scattered experimental fields are in agreement with the ideal results, and features of the total fields from the principal direction incidence trials can be seen combined in the total field from the 45° incidence trial (e.g. stronger reflection in the x-direction than the y-direction).

Some error is more noticeable than in the κ_{eff} results, particularly in the scattered phase data. For the 0° and 45° incidence trials, the experimental scattering lags the ideal in the reflected region, while leading it in the transmitted region. We attribute this error to asymmetry in the unit cell design, specifically that the speakers are off to the side of the particle velocity sensing microphone pairs and that they do not act as ideal dipoles (the amplitude is slightly larger on one side than the other). A consequence of this can be seen in the x-direction total field plot, where the non-ideal phase of the scattered waves shifted the standing waves in the reflected region closer to the metamaterial and resulted in increased shadowing in the transmitted region. This error could be minimized with a more symmetric unit cell design. It is still clear that the programming strategy of equation (4) effectively realized the desired $\widetilde{\boldsymbol{\rho}}$.

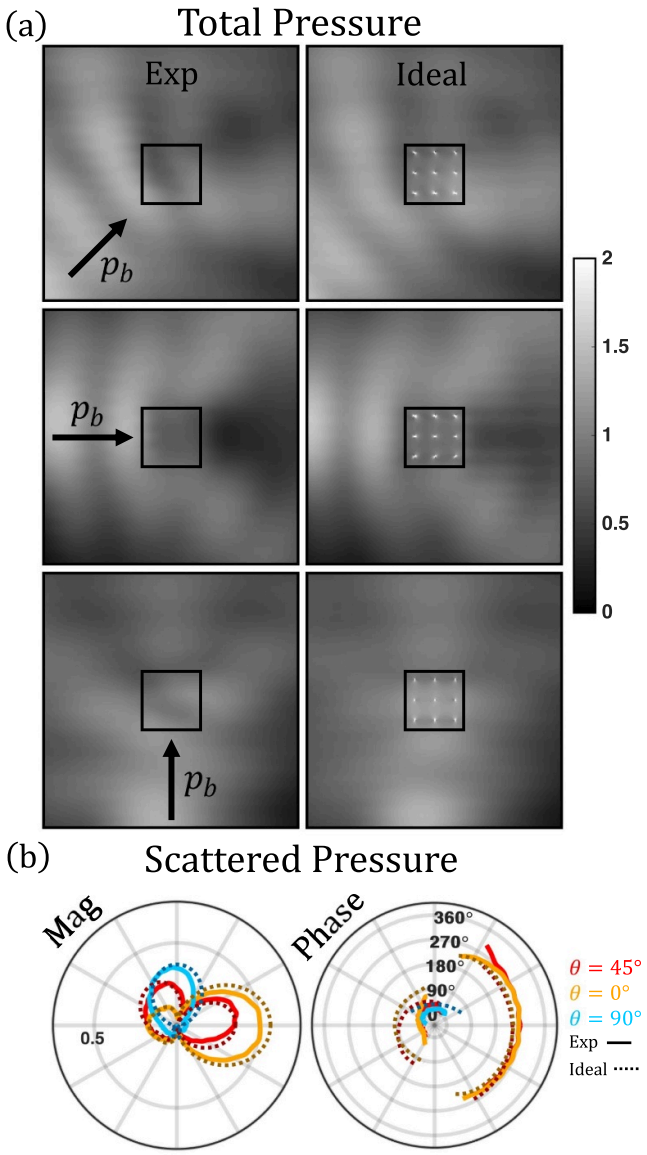

Figure 3. Comparison of experimental and simulated ideal pressure fields due to a 45°, 0°, and 90° background wave incident on the metamaterial programmed with $\rho_{\text{eff},x} = 0.5$ and $\rho_{\text{eff},y} = 1.5$. (a) Total pressure magnitudes in a 60 cm square area with the metamaterial indicated by a black outline. (b) Scattered pressure magnitudes and phases along a 40 cm diameter circle centered on the metamaterial.

3.3. Non-diagonal anisotropic mass density tensor and full programming

Even though the dipole speakers and microphone pairs are fixed in the x- and y-directions, the full mass density tensor $\boldsymbol{\rho}$ can still be programmed by using all four of the dipole gains in equation (2) that constitute the dipole gain tensor $\boldsymbol{g}^{(d)}$. This enables rotations of the principal axes of anisotropy as well as non-reciprocal behavior through the tensor asymmetry $\rho_{xy} \neq \rho_{yx}$. However, we cannot immediately map from the desired $\boldsymbol{\rho}$ to $\boldsymbol{g}^{(d)}$ because equation (4) is nonlinear. To program an arbitrary mass density tensor with individually specified elements, we first diagonalize $\boldsymbol{\rho}$ as $\widetilde{\boldsymbol{\rho}} = \boldsymbol{P}^{-1}\boldsymbol{\rho}\boldsymbol{P}$, where $\boldsymbol{P}$ is the matrix with right eigenvectors of $\boldsymbol{\rho}$ as columns and $\boldsymbol{P}^{-1}$ is its inverse. Then, we can use equation (4) to find the diagonal gain tensor $\widetilde{\boldsymbol{g}}^{(d)}$ corresponding to $\widetilde{\boldsymbol{\rho}}$ as in the previous section. Lastly, we rewrite $\widetilde{\boldsymbol{g}}^{(d)}$ in the Cartesian basis as $\boldsymbol{g}^{(d)} = \boldsymbol{P}\widetilde{\boldsymbol{g}}^{(d)}\boldsymbol{P}^{-1}$, where $\boldsymbol{g}^{(d)}$ is fully populated. Physically, this means that the dipole speakers now also have coupling to the particle velocities in the orthogonal directions. We can theoretically program any desired $\boldsymbol{\rho}$ using this method.

For an experimental demonstration that is applicable to the realization of transformation acoustics devices, we programmed the metamaterial with $\kappa_{\text{eff}} = 0.75$ and a symmetric $\boldsymbol{\rho}$ with principal axes rotated $\phi = 60°$ from the anisotropic $\widetilde{\boldsymbol{\rho}}$ demonstrated in the previous section. This transformation would be particularly challenging to achieve with passive metamaterials, as unit cells in a square array cannot be physically rotated without overlapping structures and misaligning the acoustic wave propagation paths. Therefore, the passive unit cell design must occur at the level of the full device, while the active unit cells can simply be considered independently.

In the Cartesian frame, our rotated $\boldsymbol{\rho}$ of interest has the components $\rho_{\text{eff},x} = 1.25$, $\rho_{\text{eff},xy} = \rho_{\text{eff},yx} = -0.43$, $\rho_{\text{eff},y} = 0.75$. We could map this to $\boldsymbol{g}^{(d)}$ using the diagonalization method, but because we previously found $\widetilde{\boldsymbol{g}}^{(d)}$, we can instead perform the rotation transformation directly,

$$\boldsymbol{g}^{(d)} = \boldsymbol{Q}\widetilde{\boldsymbol{g}}^{(d)}\boldsymbol{Q}^{-1}, \quad \boldsymbol{Q} = \begin{bmatrix} \cos\phi & -\sin\phi \\ \sin\phi & \cos\phi \end{bmatrix}, \tag{5}$$

where $\boldsymbol{Q}$ is the 2D rotation matrix for the rotation angle ϕ and $\boldsymbol{Q}^{-1}$ is its inverse.

The total field due to 45° incidence on the metamaterial can be seen in figure 4(a), along with the associated scattered field in figure 4(b). The experimental and ideal results are in agreement with a similar degree of error to those of the previous section. We have now shown the ability to independently program the bulk modulus κ and the full mass density tensor $\boldsymbol{\rho}$.

3.4. Impedance-matched lossy layer

In equations (3) and (4), the programmed phase required for real effective properties is either 0° or 180°. The programming-property relationships are actually also valid for complex effective properties, enabling the specification of loss or gain behavior. One application of this is the realization of a layer that absorbs incident waves without reflection. Due to the limited width of our experimental metamaterial, we will only demonstrate such a layer under the condition of normal incidence. The required effective characteristic impedance is $z_{0,\text{eff}} = 1$ and the effective speed of sound c_{eff} must have a positive imaginary component (assuming a positive phase velocity). For simplicity, we chose $|c_{\text{eff}}| = 1$, yielding the necessary bulk modulus and mass density $\kappa_{\text{eff}} = 1e^{j\alpha}$ and $\rho_{\text{eff}} = 1e^{-j\alpha}$, where $0° < \alpha < 90°$. Higher values of α will cause

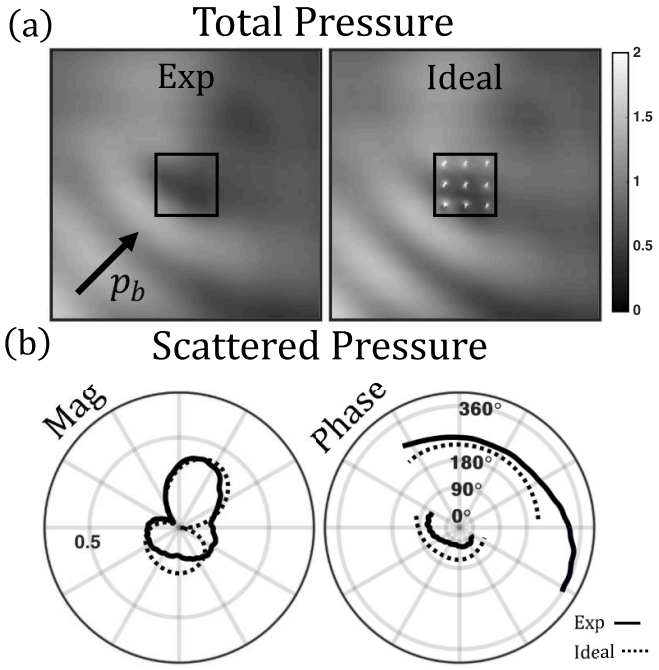

Figure 4. Comparison of experimental and simulated ideal pressure fields due to a 45° background wave incident on the metamaterial programmed with $\kappa_{\text{eff}} = 0.75$ and $\rho_{\text{eff},x} = 1.25$, $\rho_{\text{eff},xy} = \rho_{\text{eff},yx} = -0.43$, $\rho_{\text{eff},y} = 0.75$. (a) Total pressure magnitudes in a 60 cm square area with the metamaterial indicated by a black outline. (b) Scattered pressure magnitudes and phases along a 40 cm diameter circle centered on the metamaterial.

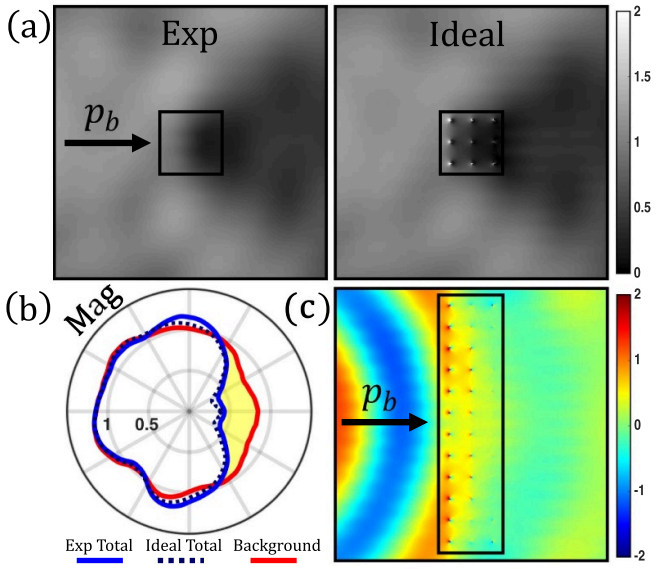

Figure 5. Performance of the metamaterial programmed as an impedance-matched lossy layer. (a) Comparison of experimental and simulated ideal total pressure field magnitudes due to a background wave in the x-direction. (b) Total and background pressure magnitudes along a circle centered on the metamaterial, with a yellow region indicating the effect of loss. (c) Real total pressure field for an ideal metamaterial with cells added to increase its height.

incident waves to decay more steeply in the effective medium, but also necessitate larger programmed gains. For significant loss while avoiding instability due to behavior at frequencies outside of the target band, we chose to experimentally demonstrate $\alpha = 30°$.

Experimental and ideal results for incidence in the x-direction are shown in figure 5. The total pressure magnitude fields in figure 5(a) do not have standing waves in the reflected region and have clear shadowing in the transmitted region. There are some high magnitude angled areas on the top and bottom of the metamaterial due to scattering from its sides, but they are expected as the effective properties were designed only to prevent reflections from normal incidence. In figure 5(b), the experimental and ideal total pressure magnitudes are plotted in blue and background magnitude in red as a polar plot along the circular slice of figure 1(c). The total magnitudes overlap with the background magnitudes on the reflected side, indicating the absence of scattering. On the transmitted side, the total field has lower magnitude than the background field. This separation is shown as a yellow area, which can be used as a measure of loss. Lastly, figure 5(c) shows the real total pressure field given the same background field, but an ideal metamaterial with quadruple the height. This highlights the potential of the approach with more unit cells, which could easily be added to the existing metamaterial.

3.5. Measured dispersion

The metamaterial frequency response is a product of the responses of the constituent microphones, speakers, amplifiers, and programmed digital processing. In this work, we have shown that by using the simple adjustments of a scalar gain and unit delay, we can obtain the ideal responses specified by equations (3) and (4) at the target frequency of 1200 Hz and endow the metamaterial with the desired effective properties at that frequency. Without any additional digital processing to appropriately adjust the magnitude and phases of the response at other frequencies, the metamaterial behavior will be dispersive (even with ideal programming, dispersion will occur outside the regime of highly subwavelength unit cell size).

Figure 6 shows the frequency-dependent effective properties of a unit cell programmed for $\kappa_{\text{eff}} = 2$ and $\rho_{\text{eff}} = 0.5$, as was implemented in the previous sections. The complex property values were obtained by measuring the experimental frequency response of the unit cell in the 2D waveguide and inversing equations (3) and (4). It can be seen that at 1200 Hz, the real component of the effective properties match the desired and the imaginary component is zero. Elsewhere, the cell response, which has approximately linearly decreasing phase of 360° over the plotted frequencies and some non-ideal magnitude profile, results in gradually varying properties. It is important to note that this variation is unlike the steep peaks characteristic of passive resonant metamaterials,

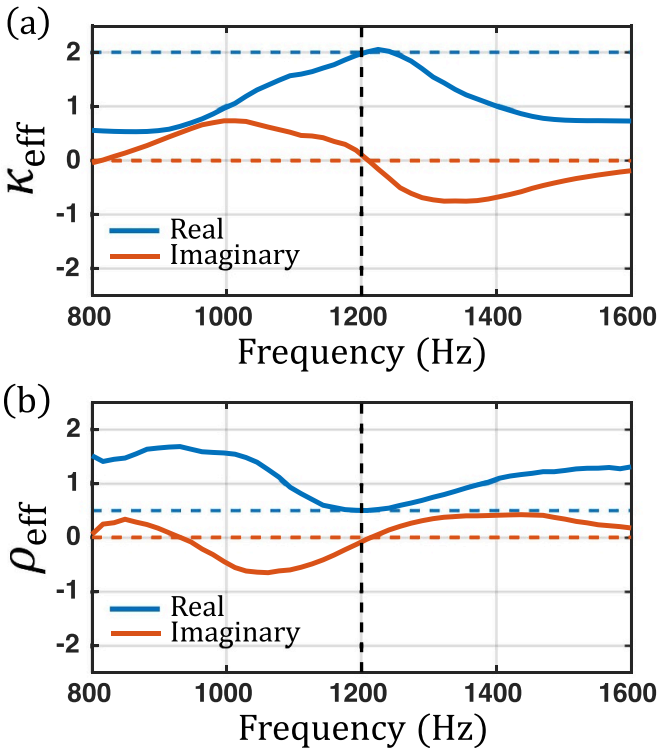

Figure 6. Frequency dependent effective properties of the metamaterial programmed for (a) $\kappa_{\text{eff}} = 2$ and (b) $\rho_{\text{eff}} = 0.5$. The real and imaginary effective property components obtained from experimentally measured frequency responses are plotted as solid lines, while the desired values are plotted as horizontal dashed lines. The target operating frequency of 1200 Hz is indicated by a vertical dashed line.

as would typically be needed to obtain $\rho_{\text{eff}} < 1$ for example. The bandwidth of the active metamaterial could be increased by minimizing the lag in the electronics, scaling the response magnitude with the square of the frequency within the operating band, and reducing the impact of unwanted feedback by decreasing the cell size or programming effective properties closer to unity.

4. Conclusion

Transformation acoustics devices have proven to be extremely difficult to realize because of their complicated material property specifications which include arbitrary pairings of bulk modulus and anisotropic mass density. In this work, we experimentally demonstrated a 2D active acoustic metamaterial composed of independently operating unit cells that can easily be programmed for desired κ and ρ using an open loop control scheme. We showcased the metamaterial performance with several example property sets that are particularly challenging to achieve through passive methods. Experimental total and scattered fields were compared to ideal fields to validate the results.

For a clear assessment of the acoustic behavior with a limited number of cells, we chose to demonstrate a metamaterial with a square geometry and homogeneous properties. However, because the cells behave independently in the design strategy we employed, they can be arranged to form a metamaterial of arbitrary geometry as well as programmed individually to achieve spatially varying properties. This is in contrast to typical active sound control methods, which require the centralized control of the active elements and a full redesign when they are reconfigured.

The range of accessible properties and bandwidth of the active acoustic metamaterial we demonstrated both depend on the ability to accurately program model frequency responses. The limitations here primarily arise from the constraints of causality and the non-ideal behavior of the physical components. High gains in frequency bands where the behavior is not passive can cause instability [41], reducing how greatly the metamaterial properties can vary from the background. However, these restrictions can be addressed through optimization of the metamaterial design, unlike for example the narrow band performance inherent to passive resonant structures. This makes active acoustic metamaterials a viable path towards devices with broadband performance, as necessary for most practical applications.

Beyond the properties required for transformation acoustics, active acoustic metamaterials can potentially be programmed to exhibit a variety of other behaviors of interest. As an example, we demonstrated a reflectionless lossy layer, but there is also a clear path to programming Willis coupling, nonreciprocity, non-Hermitian physics, and spatiotemporal modulation. While just the bulk modulus and mass density can be employed to significantly manipulate acoustic waves, the ability to implement these exotic properties would unlock additional degrees of freedom for the realization of unprecedented devices.

Data availability statement

The data that support the findings of this study are available upon reasonable request from the authors. The data cannot be made publicly available upon publication because no suitable repository exists for hosting data in this field of study.

Acknowledgments

This work was supported by the National Science Foundation under Grant No. CMMI-1942901.

ORCID iDs

Dylan A Kovacevich https://orcid.org/0000-0001-5848-0818
Bogdan-Ioan Popa https://orcid.org/0000-0003-2391-7164

References

[1] Milton G W, Briane M and Willis J R 2006 *New J. Phys.* **8** 248
[2] Cummer S A 2013 *Acoustic Metamaterials: Negative Refraction, Imaging, Lensing and Cloaking* (*Springer Series in Materials Science*) ed R V Craster and S Guenneau (Springer) pp 197–218
[3] Wu L-Y, Chiang T-Y, Tsai C-N, Wu M-L and Chen L-W 2012 *Appl. Phys.* A **109** 523
[4] Wu L *et al* 2019 *Phys. Rev. Appl.* **12** 044011
[5] Dong E, Zhou Y, Zhang Y and Chen H 2020 *Phys. Rev. Appl.* **13** 024002
[6] Popa B-I and Cummer S A 2009 *Phys. Rev.* B **80** 174303
[7] Zigoneanu L, Popa B-I and Cummer S A 2011 *Phys. Rev.* B **84** 024305
[8] Bai L, Dong H Y, Song G Y, Cheng Q, Huang B, Jiang W X and Cui T J 2018 *Adv. Mater. Technol.* **3** 1800064
[9] Cummer S A and Schurig D 2007 *New J. Phys.* **9** 45
[10] Li J and Pendry J B 2008 *Phys. Rev. Lett.* **101** 203901
[11] Popa B-I and Cummer S A 2011 *Phys. Rev.* B **83** 22 224304
[12] Liang Z and Li J 2011 *Appl. Phys. Lett.* **98** 241914
[13] Fang N, Xi D, Xu J, Ambati M, Srituravanich W, Sun C and Zhang X 2006 *Nat. Mater.* **5** 452
[14] Lee S H, Park C M, Seo Y M, Wang Z G and Kim C K 2009 *Phys. Lett.* A **373** 4464
[15] Ma G and Sheng P 2016 *Sci. Adv.* **2** e1501595
[16] Cummer S A, Christensen J and Alú A 2016 *Nat. Rev. Mater.* **1** 1
[17] Zhang S, Xia C and Fang N 2011 *Phys. Rev. Lett.* **106** 024301
[18] Zigoneanu L, Popa B-I and Cummer S A 2014 *Nat. Mater.* **13** 352
[19] Bi Y, Jia H, Lu W, Ji P and Yang J 2017 *Sci. Rep* **7** 705
[20] Chen Y, Zheng M, Liu X, Bi Y, Sun Z, Xiang P, Yang J and Hu G 2017 *Phys. Rev.* B **95** 180104
[21] Popa B-I, Zigoneanu L and Cummer S A 2013 *Phys. Rev.* B **88** 024303
[22] Cho C, Wen X, Park N and Li J 2020 *Nat. Commun.* **11** 251
[23] Akl W and Baz A 2012 *J. Appl. Phys.* **112** 084912
[24] Popa B-I, Zhai Y and Kwon H-S 2018 *Nat. Commun.* **9** 5299
[25] Zhai Y, Kwon H-S and Popa B-I 2019 *Phys. Rev.* B **99** 220301
[26] Cho C, Wen X, Park N and Li J 2021 *Commun. Phys.* **4** 1
[27] Wen X, Yip H K, Cho C, Li J and Park N 2023 *Phys. Rev. Lett.* **130** 176101
[28] Popa B-I and Cummer S A 2014 *Nat. Commun.* **5** 3398
[29] Geib N, Sasmal A, Wang Z, Zhai Y, Popa B-I and Grosh K 2021 *Phys. Rev.* B **103** 165427
[30] Zhou H and Baz A 2021 *J. Acoust. Soc. Am.* **150** 1092
[31] Zhai Y, Kwon H-S and Popa B-I 2021 *Phys. Rev. Appl.* **16** 034023
[32] Wen X, Zhu X, Fan A, Tam W Y, Zhu J, Wu H W, Lemoult F, Fink M and Li J 2022 *Commun. Phys.* **5** 1
[33] Popa B-I, Shinde D, Konneker A and Cummer S A 2015 *Phys. Rev.* B **91** 220303
[34] Wen X, Zhu X, Wu H W and Li J 2021 *Phys. Rev.* B **104** L060304
[35] Li X, Chen Y, Hu G and Huang G 2018 *Smart Mater. Struct.* **27** 045015
[36] Chen Y, Li X, Nassar H, Hu G and Huang G 2018 *Smart Mater. Struct.* **27** 115011
[37] Li X, Chen Y, Zhang X and Huang G 2020 *Extreme Mech. Lett.* **39** 100837
[38] Wu Q, Xu X, Qian H, Wang S, Zhu R, Yan Z, Ma H, Chen Y and Huang G 2023 *Proc. Natl Acad. Sci.* **120** e2209829120
[39] Kovacevich D A and Popa B-I 2021 *Phys. Rev.* B **104** 134304
[40] Kovacevich D A and Popa B-I 2022 *Appl. Phys. Lett.* **121** 101701
[41] Kovacevich D A, Grosh K and Popa B-I 2024 *Phys. Rev. Appl.* **21** L051002